Editors' Suggestion

Formation of Complex Spin Textures in Thermally Demagnetized $La_{0.7}Sr_{0.3}MnO_3$ Artificial-Spin-Ice Structures

Dayne Y. Sasaki,[1] Rajesh V. Chopdekar,[2] Scott T. Retterer,[3] Daniel Y. Jiang,[4] Jeremy K. Mason,[1] Michael S. Lee,[1] and Yayoi Takamura[1,*]

[1] *Department of Materials Science and Engineering, University of California – Davis, Davis, California 95616, USA*

[2] *Advanced Light Source, Lawrence Berkeley National Laboratory, Berkeley, California 94720, USA*

[3] *Center for Nanophase Materials Sciences, Oak Ridge National Laboratory, Oak Ridge, Tennessee 37831, USA*

[4] *Department of Chemical Engineering, University of California – Davis, Davis, California 95616, USA*

(Received 16 February 2022; revised 6 May 2022; accepted 31 May 2022; published 29 June 2022)

Artificial spin ices (ASIs) have traditionally been designed such that each nanomagnet possesses a single-domain magnetic configuration that is assumed to be minimally perturbed by interisland dipolar interactions. Using x-ray photoemission electron microscopy to perform magnetic domain imaging, we study thermally demagnetized $La_{0.7}Sr_{0.3}MnO_3$-based brickwork ASI arrays and showed that complex spin textures (CSTs) can be stabilized through an appropriate selection of nanoisland width and interisland spacing. While the width dependence can be explained through the dominance of shape anisotropy in isolated nanoislands, the ASIs we investigate demonstrate a complex dependence on both the nanoisland width and interisland spacing. Micromagnetic simulations reveal that interisland dipolar interactions play a role in the formation of CSTs, which are composed of single- and double-vortex states. Energy analysis of the simulations provides an understanding of the system energetics that arises from a delicate balance between *intra*island effects (i.e., shape anisotropy and exchange energy) and *inter*island effects (i.e., dipolar interactions between nearest-neighbor nanoislands).

DOI: 10.1103/PhysRevApplied.17.064057

I. INTRODUCTION

Artificial spin ices (ASIs) are lithographically patterned arrays of interacting single-domain magnetic nanoislands that can be represented as an ensemble of dipolar-coupled Ising macrospins that are unable to simultaneously minimize all neighboring magnetic interactions (i.e., they exist in a frustrated state). Originally introduced as an engineered analog of spin-ice crystals whose frustrated physics could be directly visualized with conventional magnetic microscopy [1], ASIs have served as a platform for designing and investigating phenomena including configurational excitations resembling magnetic monopole-like defects [2–4], phase transitions between different global nanomagnetic ordering states [5–7], and magnetically reconfigurable spin-wave dynamics [8]. In ASIs, the collective physics of the entire array is highly sensitive to the interactions between individual nanomagnetic elements (i.e., *inter*island interactions), which are influenced by the nanoisland arrangement, geometry, and magnetization. Thus, ASIs have received attention for their promising potential for developing low-power computing devices with functionalities that can be magnetically reconfigured after fabrication, such as tunable GHz-frequency dynamics in ASI-based magnonic crystals [8] and switchable gate operations in nanomagnetic logic architectures [9].

Investigations of ASI systems have traditionally used geometry-based degrees of freedom as the array geometry strongly influences the net dipolar interactions between nearest-neighboring nanoislands and, therefore, controls the collective physics in these systems. These studies have produced a wide range of ASI lattice geometries, including nanoisland assemblies constructed from square, Tetris "T block", and brick-shaped (brickwork) tilings [1,10–13]. Additionally, the interaction strength between magnetically coupled nanoislands in these arrays can be modulated through changes in both the nanoisland size as well as interisland spacing, allowing these systems to access different equilibrium configurations [14,15] or alter the system degeneracy [3,16].

A common feature that many ASI studies share is their use of the soft ferromagnetic alloy permalloy ($Ni_{80}Fe_{20}$) as the magnetic material. Permalloy possesses a near absence of magnetocrystalline anisotropy, which defines the crystallographic "easy" axis that the magnetization preferentially aligns along (i.e., all in-plane axes are equally easy)

*ytakamura@ucdavis.edu

[17]. The combined use of an elongated island geometry and nanometer-scale dimensions can be used to engineer single-domain states by preventing the formation of domain walls (approximately 100 nm in width) associated with multidomain states. In other words, the nanoislands possess a shape anisotropy that favors magnetization along the long axis of elongated nanoislands that can be represented as a macrospin within an Ising framework where the island magnetization exists in one of two states (e.g., "up" or "down"). By engineering the nanoisland shape anisotropy, it may be assumed that the type of spin texture (e.g., Ising-like or vortex) formed will be determined by the island-intrinsic (i.e., *intra*island) shape effects with negligible influence from *inter*island dipolar interactions.

While permalloy-based ASI systems have facilitated the investigation of magnetic frustration and dynamics in various array geometries, the complex oxide class of materials introduces several unique opportunities for ASI studies. Complex oxides possess charge, orbital, lattice, and spin degrees of freedom; and heterostructures or nanostructures of these materials exhibit functional properties that can be tuned using parameters such as substrate orientation, individual layer thickness, and epitaxial strain state [18,19]. The patterning of complex oxide thin films into nano- and micron-sized polygons has been shown to result in equilibrium magnetic domain structures that depend on the competition between shape and magnetocrystalline anisotropy energies as well as exchange coupling interactions at interfaces [20–24]. Thus, complex oxides introduce an opportunity to incorporate their rich variety of tunable functional properties with the designable physics of ASIs.

Additionally, complex oxides have demonstrated promise for use in thermally active ASI studies [25]. ASIs fabricated from the epitaxial complex oxide $La_{0.7}Sr_{0.3}MnO_3$ (LSMO) offer the advantage of possessing a bulk Curie temperature, $T_C \sim 370$ K (i.e., near room temperature) as well as exhibiting chemical stability up to 873 K in both vacuum and ambient pressure environments [26]. Therefore, LSMO-based ASIs can facilitate investigations of ASI ground states through thermal annealing protocols (i.e., raising the system temperature close to T_C) [27–29], unlike permalloy-based systems, which face experimental challenges such as thermal degradation imposed by high-temperature requirements (approximately 800 K) [29], or through the use of ultrathin (approximately 3 nm) nanoislands, which may be prone to variations in thickness and, consequently, blocking temperature [25].

In this paper, we report on our investigation of thermalized brickwork ASIs fabricated from the complex oxide LSMO. Using magnetic domain imaging performed using an x-ray photoemission electron microscope (XPEEM), we perform *in situ* thermal demagnetization and observe the formation of complex spin textures (CSTs), which consist of single- and double-vortex states. These states can be stabilized using *both* the nanoisland width and interisland spacing. Micromagnetic simulations demonstrate that these spin textures consist predominantly of single- and double-vortex states. The simulations also provide an understanding of their energetics, which arises from a competition between *intra*island effects (i.e., shape anisotropy and exchange energy) and *inter*island effects (i.e., magnetostatic interactions between nearest-neighbor nanomagnets). By constructing a width- and spacing-dependent phase diagram from the simulated energy surfaces, we find a correlation between the experimentally observed CST abundance and the associated energetic preference of Ising or CST states.

II. METHODS

A 40-nm-thick LSMO film is grown epitaxially on a (001)-oriented Nb-doped $SrTiO_3$ (0.05 wt % Nb) substrate using pulsed laser deposition with a laser fluence of approximately 1 J cm^{-2} and frequency of 1 Hz. During the growth, the substrate temperature is held at 700 °C with an oxygen pressure of 0.3 Torr. The film is slowly cooled to room temperature postdeposition in 300 Torr O_2 to ensure proper oxygen stoichiometry. Structural characterization is performed with x-ray reflectivity and x-ray diffraction to confirm coherent growth, crystalline quality, and thickness of the film (for details, see Ref. [25]). ASI arrays are defined in different regions of a single LSMO film using a patterning technique based on the local modification of the structural and magnetic order by a flood Ar^+ ion implantation (for details, see Refs. [20,30]). Each ASI array contained over 900 stadium-shaped nanoislands (rectangles with semicircle endcaps) with a fixed length of 470 nm and widths, W, varying from 100 to 175 nm to control the nanoisland moment, m. These nanoislands are patterned such that the two-dimensional ⟨10⟩ axes of the ASI are aligned with the ⟨110⟩ in-plane easy axes of the LSMO film under tensile strain [31]. The spacing between each nanomagnet is modified through the ASI lattice parameter, a, where each three-island vertex in the brickwork structure [Fig. 1(a)] corresponds to a point in a square lattice (henceforth any discussions associated with lattices will only be associated with the ASI and not the LSMO crystal structure). By varying the value of a from 600 to 650 nm, we are able to fine tune the interisland coupling strength, $J \equiv m^2/a^3$, which reflects the scale of dipolar interaction [15]. Each unique combination of a and W has been listed in Table I and assigned a unique letter. The observed CST populations for each array are also listed in Table I and are discussed in greater detail below. We note that for each ASI in Table I, two duplicate arrays are fabricated at different regions on the same LSMO film.

Magnetic domain imaging is performed using XPEEM using the PEEM-3 endstation at beamline 11.0.1.1 of

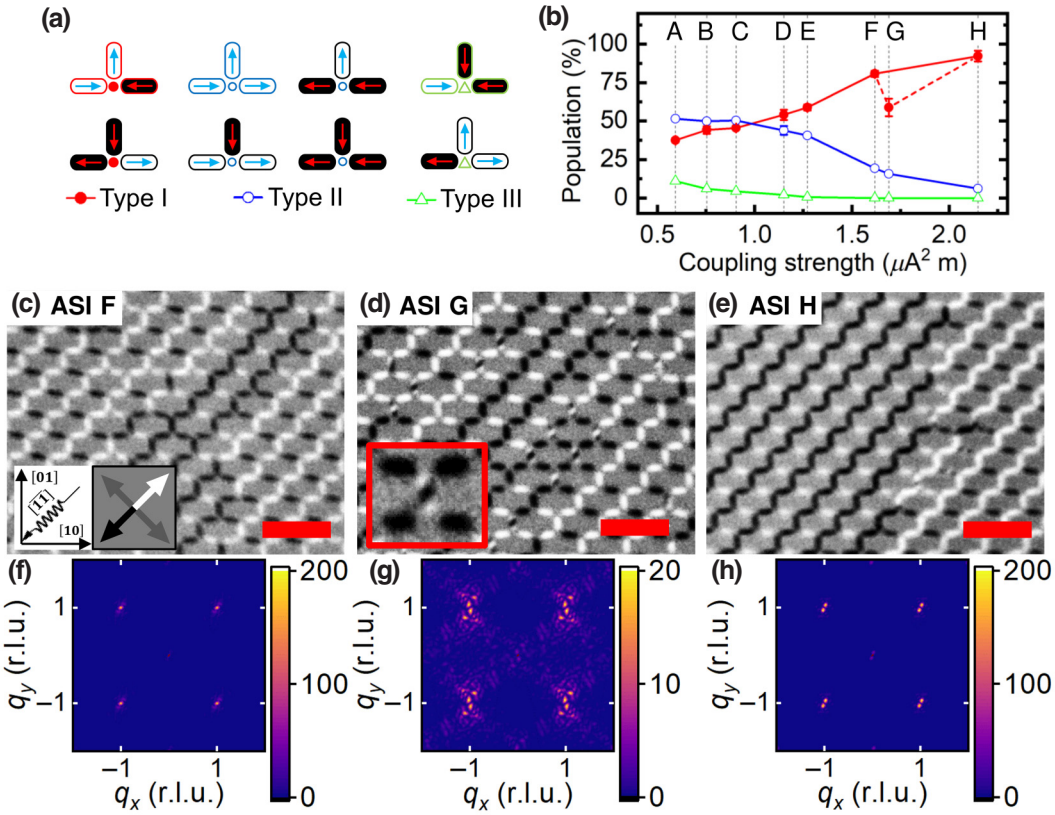

FIG. 1. (a) Schematic of the eight possible Ising-like moment configurations at a three-nanoisland vertex. Type I, II, and III vertices are designated as red solid circles, blue open circles, and green triangles, respectively. (b) Average vertex population for ASIs A–H plotted as a function of coupling strength, J. Each error bar corresponds to the standard deviation between two to four unique XMCD PEEM images of the ASIs. In ASI G, the Ising model breaks down as the magnetic configuration of $9\% \pm 2\%$ of the nanoislands cannot be classified as single domains, causing a deviation in the type I population trend as indicated by the dashed line. (c)–(e) XMCD PEEM images and (f)–(h) corresponding MSF calculations of ASI F (c), (f), ASI G (d), (g), and ASI H (e), (h), respectively. The experimental geometry and associated magnetic contrasts are schematically shown on the legends. The inset in (d) shows an enlarged image of a multidomain nanoisland with contrast enhanced for visual clarity. MSFs are calculated by assuming an Ising model where CST islands possess zero net moment. Red scale bars are 2 μm. r.l.u., reciprocal lattice units, based on a square ASI lattice.

the Advanced Light Source [32]. By using circularly polarized x rays, a magnetic signal can be acquired through x-ray magnetic circular dichroism (XMCD). The circularly polarized x rays are oriented in plane along the $[\bar{1}1]$ axis of the ASI with a 30° incidence angle relative to the sample surface. XPEEM images are acquired at a photon energy corresponding to the maximum XMCD intensity at the Mn L_3 edge using right and left circularly polarized (RCP and LCP) x rays. Other sources of contrast (i.e., local work-function differences or topography) are minimized by performing an asymmetry calculation, $I = (I_{\mathrm{RCP}} - I_{\mathrm{LCP}})/(I_{\mathrm{RCP}} + I_{\mathrm{LCP}})$, where I_{RCP} and I_{LCP} correspond to the pixelwise intensities from images acquired using RCP and LCP x rays, respectively. The

TABLE I. Geometric parameters and CST populations of brickwork ASI.

ASI	Island width, W (nm)	Lattice parameter, a (nm)	Unique images acquired	Coupling strength, J (μA^2 m)	CST population
A	100	650	4	0.59	0%
B	100	600	4	0.75	0%
C	125	650	4	0.91	0%
D	125	600	4	1.15	0%
E	150	650	3	1.27	0%
F	150	600	2	1.62	0%
G	175	650	4	1.69	$9\% \pm 2\%$
H	175	600	4	2.15	$0.5\% \pm 0.6\%$

XMCD contrast depends as $\cos(\theta)$ where θ is the angle between the nanoisland magnetization relative to the x-ray helicity vector and thus XMCD PEEM images are sensitive only to the projection of the local magnetization onto the direction of the incident x-ray beam [33]. X-ray absorption (XA) images, which possess information about the sample topography, are also produced by averaging the polarizations, $I = (I_{\mathrm{RCP}} + I_{\mathrm{LCP}})/2$. After a thermal demagnetization protocol, the sample temperature is set to 110 K to maximize the XMCD contrast and minimize thermally induced magnetization evolution.

To analyze the images within the traditionally utilized Ising framework, we develop an analysis routine based on the OpenCV implementation of the Earth Movers Distance used in image classification [34,35]. This routine automated the detection of nanoisland locations and magnetization directions. To quantitatively understand the J-dependent ordering behavior of the ASIs, the routine determined the populations of different vertex configurations [Fig. 1(b)], which is discussed in further detail below. Additionally, the routine determined the reciprocal space magnetic structure factors (MSFs) of the ASI arrays, which is equivalent to a magnetic diffraction pattern of the ASI. MSFs are calculated by the method described by Östman *et al.* [36]. For determining vertex types and MSFs, nanoislands with spin textures more complicated than single domains are assumed to possess a zero net moment.

Micromagnetic simulations are performed with MuMax^3, which calculates the lowest energy state of magnetic features in a ferromagnetic system using the Landau-Lifshitz-Gilbert equation and outputs a full vector field of the local magnetization that can be represented as a color map [37]. We also process the simulated magnetization vector fields to produce images that are representative of both the experimental geometry and resolution of the PEEM-3 microscope. LSMO input parameters at approximately 110 K included the exchange stiffness, $A_{\mathrm{ex}} = 3.6$ pJ/m, saturation magnetization, $M_{\mathrm{sat}} = 390$ kA/m, and magnetocrystalline anisotropy constant, $K_1 = 0$ kJ/m^3 for magnetic nanoislands patterned using the ion-implantation-based technique [22]. The simulated cell volume size is set to $2.5 \times 2.5 \times 40$ nm^3 where we assume uniform magnetization throughout the nanoisland thickness. The lateral cell dimensions fall below the magnetostatic exchange length of $l_s = \sqrt{2A_{\mathrm{ex}}/(\mu_0 M_{\mathrm{sat}}^2)} = 6.14$ nm. The region between the nanoislands is modeled to be empty space as the paramagnetic matrix between nanoislands in our ASIs possess a permeability close to that of vacuum ($\mu_r \sim 1.1$) [25].

To examine the magnetic interactions of the nanoislands in the absence of any external magnetic fields, the ASIs are thermally annealed by heating the sample in the PEEM-3 endstation on a nonmagnetic sample holder to 350 K, which is above the experimentally determined Curie temperature of the LSMO thin film ($T_C \sim 338$ K, Ref. [25]). The sample is subsequently cooled to the measurement temperature of 110 K at a rate of approximately 5 K/min [25]. The sample is thermally annealed twice *in situ* at PEEM-3 and the ASI arrays are imaged after each annealing procedure. Since this sample contains two duplicates of each unique ASI, we collect two to four unique XMCD PEEM images of the nanoisland magnetization [e.g., Figs. 1(c)–1(e)] for each ASI configuration, which are used to calculate statistics. All error bars discussed in this work correspond to the standard deviation between the XMCD PEEM images.

III. RESULTS AND DISCUSSION

In XMCD PEEM images, domains magnetized parallel, antiparallel, or perpendicular to the x-ray helicity appear as regions with black, white, or gray contrast, respectively. Our analysis routine automatically determined the nanoisland locations, magnetization directions, and vertex types from the XA and XMCD PEEM images. The population of vertex types is used to quantitatively describe the magnetic configurations in ASI systems. Each three-nanoisland vertex in the brickwork ASI is classified based on its net dipolar interaction energy described by

$$E_{\mathrm{dipolar}} = \sum_{i<j}^{N} \frac{\mu_r \mu_0}{4\pi r_{ij}^3} \left[\mathbf{m_i} \cdot \mathbf{m_j} - \frac{3(\mathbf{m_i} \cdot \mathbf{r_{ij}})(\mathbf{m_j} \cdot \mathbf{r_{ij}})}{r_{ij}^2} \right], \tag{1}$$

where $\boldsymbol{m_i}$ is the ith nanoisland moment, $\boldsymbol{r_{ij}}$ is the center-to-center vector between nanoislands, and μ_r is the relative permeability of the matrix region between the nanoislands ($\mu_r \sim 1.1$ at room temperature, Ref. [25]). Out of the $2^3 = 8$ possible nanoisland magnetization directions available at each vertex, three sets of degenerate vertex types exist [Fig. 1(b)] that are labeled based on their relative energies (i.e., $E_{\mathrm{I}} < E_{\mathrm{II}} < E_{\mathrm{III}}$). Within the traditional Ising framework, the prevalence of each vertex type depends on J. As shown in Fig. 1(b), brickwork ASIs with small values of J (e.g., ASI A) possess randomized nanoisland magnetization directions and vertex population values representative of their multiplicities (i.e., 25% for type I, 50% for type II, 25% for type III). As a consequence, the MSF of the disorderly arrays possess weak and broadened peaks (see Fig. S1 within the Supplemental Material [38]). As J increases (by increasing W or decreasing a), the ASIs establish longer-ranged ordering characterized by extended stairlike steps with white or black XMCD contrast in Figs. 1(c) and 1(e), increased population of type I vertices, and sharp, well-defined peaks in the MSF [Figs. 1(f) and 1(h)].

Analysis of the XMCD PEEM images indicated that nanoislands in ASI A through F are all single-domain states while nanoislands in ASI G and H possess a majority Ising-like nanomagnets and a small percentage of CSTs,

which are assigned to have zero-net moment in statistical and MSF calculations. Only $0.5\% \pm 0.6\%$ of the nanoislands in ASI H formed CSTs while $9\% \pm 2\%$ are observed in ASI G with nearly identical population across all four images acquired. Consequently, $25\% \pm 5\%$ of the vertices in ASI G are flanked by CST-bearing nanoislands and could not be classified as a type I–III vertex, in comparison to $2\% \pm 2\%$ of the vertices in ASI H.

CST formation in LSMO-based ASIs depends strongly on the local geometric environment. In ASI G (i.e., ASI with largest CST abundance), approximately 95% of CST-bearing nanoislands are vertically oriented. Conversely, square ASI arrays (i.e., the parent configuration of brickwork ASI without the removal of select nanoislands) with identical island size and ASI lattice spacing possessed only approximately 1% CSTs (see Fig. S4 within the Supplemental Material [38]) on the same LSMO thin-film sample as in this study, as well as in an identical square ASI studied in Ref. [25]. Note that the labels assigned to square ASIs in Fig. S4 within the Supplemental Material [38] correspond with a and W values listed in Table I. While each nanoisland in square ASIs possesses identical nearest-neighbor configurations, in brickwork ASIs, the vertical [01]-oriented and horizontal [10]-oriented nanoislands differ in their nearest-neighbor configurations and, thus, are subjected to distinct dipolar interaction environments. As shown in Fig. S5 within the Supplemental Material [38], the horizontal brickwork ASI nanoislands possess first- (NN^1) and second-nearest-neighbor (NN^2) nanoislands that are similar in their geometric environment compared to those found in the parent square ASI [38]. The NN^1 and NN^2 nanoislands surround the same vertices as the reference nanoisland with either perpendicular or parallel orientation, respectively. In comparison, the vertical nanoislands in brickwork ASIs are only flanked by perpendicularly oriented NN^1 nanoislands. This correlation between nearest-neighbor configurations and CST formation probabilities demonstrates the sensitivity of CST formation on the local geometric environment, which therefore influences the local dipolar interactions.

Analysis of XA PEEM images indicates that no significant differences existed in terms of nanoisland size, spacing, or edge imperfections, ruling out local changes in the nanoisland shape or dipolar coupling due to lithographic errors as factors inducing CST formation. These CSTs did not appear exclusively within certain nanoislands after repeated thermal demagnetization steps (see Fig. S3 within the Supplemental Material [38]). Furthermore, similar CST formation behavior is observed in ASIs patterned in subsequent LSMO-based samples using similar widths and lattice spacing. Therefore, the behavior of ASI G can be considered to be inherent to this system with its unique combination of a and W values as well as nanoisland geometry, and not an anomaly within a particular sample.

Unlike ASI F [Fig. 1(c)] and H [Fig. 1(e)], which both demonstrate long-range magnetic ordering, images of ASI G [Fig. 1(d)] show a stark reduction in long-range magnetic ordering with only small patches of the low-energy ground-state Ising configuration. This observable change in the real-space magnetization ordering in ASI G also corresponds to peak broadening and an order of magnitude reduction in peak intensity in the MSF [Fig. 1(g) and Figs, S1 and S2 within the Supplemental Material [38]] . Furthermore, an abrupt deviation in type I vertex population is observed only in ASI G in Fig. 1(b), which may be associated with both the reduction of long-range ordering and the inability to apply the Ising model to vertices with CST nanoislands.

The XMCD PEEM images suggest the presence of two types of CST observed in ASI H and G. These CSTs appear as three [Fig. 2(a)] or two [Fig. 2(b)] regions with alternating contrast separated by transition regions of approximately 50 nm in width oriented along the ASI [11] axis. Kim *et al.* investigated similarly sized rectangular and elongated hexagonal LSMO nanoislands and suggested that these spin textures corresponded to flux-closure states when taking into account the limited lateral resolution of the PEEM-3 microscope for complex oxide samples [23]. MuMax^3 micromagnetic simulations [37], with Gaussian blurring to simulate actual experimental resolution limits, confirmed that the XMCD PEEM contrast pattern can arise from the magnetization projection of single- and double-vortex spin textures as shown in Fig. 2. The gradual rotation of the local magnetization

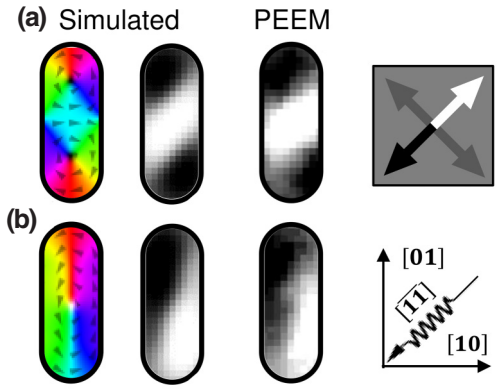

FIG. 2. (a), (b) Simulated (left and center) and XMCD PEEM (right) images of the double (a) and single (b) vortex spin textures. The colored regions in the vector field map (left) represent the in-plane component of the magnetization (also indicated by the arrows). The simulated XMCD images in the center are processed to reflect both the experimental geometry and resolution (see text for processing details). The contrast in both PEEM and simulated XMCD images is enhanced for visual clarity. Schematics of the experimental geometry and associated magnetic contrast for both PEEM and simulated images are shown in the far right.

in such CSTs is consistent with a magnetic material with minimal magnetocrystalline anisotropy, as is the case with these LSMO nanoislands patterned through ion implantation [22].

The formation of spin textures in isolated magnetic nanoislands is typically explained as a balance between magnetostatic (E_{MS}), exchange (E_{exch}), and magnetocrystalline anisotropy energies. For the elongated stadium-shaped nanoislands studied in this work (aspect ratios ranging from 1:4.7 in ASI A and B to 1:2.7 in ASI G and H), E_{MS} is expected to dominate leading to single-domain magnetic configurations. The presence of CSTs in ASI G and H ($W = 175$ nm) and their absence in ASI A through F ($W \leq 150$ nm) can be partially explained by considering *intra*island energetics: as W increases, the tendency to form vortexlike states also increases since (1) E_{MS} of a single-domain state increases with greater nanoisland volume, and (2) the E_{exch} penalty for formation of a vortex state (approximately 50 eV from micromagnetic simulations) becomes smaller than the total reduction in E_{MS}.

However, *intra*island energetics alone do not explain how a values influence CST formation. Our experimental results suggest that shape anisotropy alone may be insufficient to fully predict spin-texture formation in ASI arrays and we must consider the competition between *inter*island effects (i.e., dipolar interactions) and *intra*island effects (e.g., shape anisotropy and exchange energy). To this end, we use MuMax[3] micromagnetic simulations to calculate the energies of relaxed nanomagnetic states shown schematically as Fig. 3(a) as a function of a, W, Ising magnetization of the first nearest neighbors, M_{NN}, and center island magnetization, M_{center}. The variations in a ($95\text{ nm} \leq a \leq 200$ nm) and W ($595\text{ nm} \leq W \leq 705$ nm) are performed in increments of 5 nm. M_{NN} is initialized to possess uniform magnetization that reflect the magnetization configurations observed around CSTs in XMCD PEEM images. M_{center} is initialized to possess either an Ising state or a CST state with a single or double vortex. The different configurations of the five-island unit in Fig. 3(a) are referred to as "Ising" or "CST states" depending on the magnetization state of M_{center}.

To compare the relative energies between CST and Ising states, we calculate the energy difference ΔE of the total energy (E) relative to a configuration consisting of two type I vertices, $E_{dual\,I}$, as

$$\Delta E = E(a, W, M_{NN}, M_{center}) - E_{dual\,I}(a, W) \qquad (2)$$

$E_{dual\,I}$ is found to be the ground-state energy for the range of a and W values used in our XMCD PEEM experiments. Figure 3(b) plots the minimum value of ΔE as a function of a and W. The black border separates the energy surface into two regions where the minimum ΔE is associated with an Ising state ($\Delta E_{Ising} < \Delta E_{CST}$) or a CST state ($\Delta E_{Ising} \geq \Delta E_{CST}$). Figure 3(b) shows that an intermediate range of a ($595\text{ nm} \leq a \leq 705$ nm) and W ($95\text{ nm} \leq W < 150$ nm) exists where the formation of Ising states is preferred over CSTs. For larger values of a and W above the black border, CST states became energetically favorable over an arrangement of Ising states in high-energy type II and III vertex configurations. Energetic analysis demonstrates that E_{MS} (approximately 100 eV) dominated over E_{exch} (approximately 10 eV) and that CST states became energetically preferred over Ising states only when the reduction in E_{MS} exceeded the E_{exch} penalty of approximately 50 eV. While E_{MS} depends on W, which influences the *intra*island energetics of isolated nanoislands as discussed earlier, in ASIs, E_{MS} is also influenced by a, which changes the dipolar interactions of the full array. For nanoislands experiencing attracting ("heads-to-tails") interactions, as is the case for the minimum ΔE states, E_{MS} increases with a [39,40]. However, E_{MS}, and thus ΔE, demonstrates stronger dependence on W compared to a, where E_{MS} saturates as $a \to \infty$ (i.e., nanoislands become fully isolated).

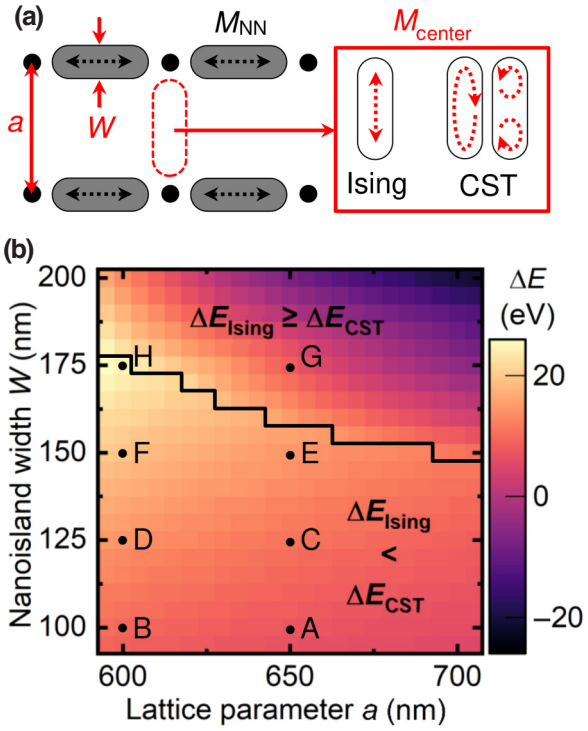

FIG. 3. (a) Schematic of the five-island unit simulated to determine the relative energies when the red center nanoisland takes on an Ising or CST state (i.e., single or double vortex). Each nearest-neighbor magnetization (M_{NN}) can have two possible orientations. (b) Minimum energy surface calculated relative to a configuration with two type I vertices, $E_{dual\,I}$ [Eq. (2)]. The black line separates the regions where the minimum ΔE is associated with an Ising M_{center} ($\Delta E_{Ising} < \Delta E_{CST}$) or a CST M_{center} ($\Delta E_{Ising} \geq \Delta E_{CST}$). Letters correspond to the ASI configurations listed in Table I.

By overlaying the ASI configurations in Table I over Fig. 3(b), we find a correlation between the CST populations observed in XMCD PEEM images and the M_{center} state associated with the minimum ΔE. For ASI A through F, CSTs are absent in the arrays and are predicted to favor Ising states over CST states ($\Delta E_{\text{Ising}} < \Delta E_{\text{CST}}$). ASI G sits well inside the region where CST states are preferred over type II and III formation ($\Delta E_{\text{Ising}} > \Delta E_{\text{CST}}$) and possess the highest CST population of $9\% \pm 2\%$. ASI H resides on the border separating the two energy regions and displays a small CST population ($0.5\% \pm 0.6\%$). This correlation between the CST populations and the associated energetic preference of Ising or CST states suggests that our micromagnetic model captures the fundamental aspects of spin-texture energetics in LSMO-based brickwork ASI. This correlation also suggests the possibility for using a and W values within the CST-preferred region ($\Delta E_{\text{Ising}} > \Delta E_{\text{CST}}$) to investigate the kinetics of CST-Ising domain formation and ASI magnetic ordering, which can be achieved by annealing our LSMO-based ASIs below its experimentally determined $T_C \sim 338$ K (Ref. [25]). Additionally, we anticipate that the application of an external magnetic field (i.e., introducing Zeeman energy into our model) may change the border location in our phase diagram as a function of field strength and direction. For instance, the border may move upwards (more a and W values favoring Ising states) with increasing field strength along the $\langle 11 \rangle$ directions as the ASI nanoislands become saturated. Both temperature- and field-dependent studies of spin-texture energetics and kinetics would provide greater insights into how specific domain-state populations can be engineered in LSMO-based ASIs.

IV. CONCLUSIONS

In conclusion, using a combination of XMCD PEEM imaging and micromagnetic simulations, we demonstrate that the formation of CSTs in LSMO-based ASIs could be tuned through the balance of both the nanoisland aspect ratio and dipolar interaction based on the configuration and spacing of the nearest-neighboring nanoislands. Energy analysis suggests that while the magnetostatic energy dominates the a- and W-dependent energetics, the small contribution from exchange energy determines whether nanoislands will preferentially form Ising or CST states. Additionally, the nanoisland magnetic state changes the magnetostatics arising from both *intra*island shape anisotropy and *inter*island dipolar interaction. These tunable nanoisland domain states provide opportunities for introducing exotic phase transitions in existing and unexplored ASI arrays which take into account the additional ways that the nanoislands interact [13]. Furthermore, the observation of tunable CST formation in LSMO-based ASIs arises from a special balance between the *inter*- and *intra*island energetics, which are enabled by the LSMO magnetic parameters. Our findings highlight the potential for materials-driven ASI studies to provide deeper insights into ASI and domain formation physics. These studies could involve ASIs patterned into complex oxide thin films and heterostructures to investigate exchange interactions in ferromagnetic and ferromagnetic (e.g., $La_{0.7}Sr_{0.3}CoO_3$/LSMO [41,42]) or antiferromagnetic and ferromagnetic ($La_{1-x}Sr_xFeO_3$/LSMO [21,24]) interfaces, strain-controlled magnetism in ferroelectric and ferromagnetic systems (e.g., $BaTiO_3$/LSMO [43]), or optically tunable ferromagnetism in LSMO coated with the halide perovskite $CH_3NH_3PbI_3$ [44].

ACKNOWLEDGMENTS

Portions of this work is supported by the National Science Foundation (Grant No. DMR 1745450). This research uses resources of the Advanced Light Source, which is a Department of Energy (DOE) Office of Science User Facility under Contract No. DE-AC02-05CH11231. E-beam lithography is performed at the Center for Nanophase Materials Sciences, which is a US DOE Office of Science User Facility.

[1] R. F. Wang, C. Nisoli, R. S. Freitas, J. Li, W. McConville, B. J. Cooley, M. S. Lund, N. Samarth, C. Leighton, V. H. Crespi, and P. Schiffer, Artificial "spin ice" in a geometrically frustrated lattice of nanoscale ferromagnetic islands, Nature **439**, 303 (2006).

[2] S. Ladak, D. E. Read, G. K. Perkins, L. F. Cohen, and W. R. Branford, Direct observation of magnetic monopole defects in an artificial spin-ice system, Nat. Phys. **6**, 359 (2010).

[3] A. Farhan, M. Saccone, C. F. Petersen, S. Dhuey, R. V. Chopdekar, Y. L. Huang, N. Kent, Z. Chen, M. J. Alava, T. Lippert, A. Scholl, and S. van Dijken, Emergent magnetic monopole dynamics in macroscopically degenerate artificial spin ice, Sci. Adv. **5**, eaav6380 (2019).

[4] L. J. Heyderman and R. L. Stamps, Artificial ferroic systems: Novel functionality from structure, interactions and dynamics, J. Phys.: Condens. Matter **25**, 363201 (2013).

[5] V. Kapaklis, U. B. Arnalds, A. Harman-Clarke, E. T. Papaioannou, M. Karimipour, P. Korelis, A. Taroni, P. C. W. Holdsworth, S. T. Bramwell, and B. Hjörvarsson, Melting artificial spin ice, New J. Phys. **14**, 035009 (2012).

[6] L. Anghinolfi, H. Luetkens, J. Perron, M. G. Flokstra, O. Sendetskyi, A. Suter, T. Prokscha, P. M. Derlet, S. L. Lee, and L. J. Heyderman, Thermodynamic phase transitions in a frustrated magnetic metamaterial, Nat. Commun. **6**, 8278 (2015).

[7] J. Sklenar, Y. Lao, A. Albrecht, J. D. Watts, C. Nisoli, G. W. Chern, and P. Schiffer, Field-induced phase coexistence in an artificial spin ice, Nat. Phys. **15**, 191 (2019).

[8] M. T. Kaffash, S. Lendinez, and M. B. Jungfleisch, Nanomagnonics with artificial spin ice, Phys. Lett. A **402**, 127364 (2021).

[9] H. Arava, P. M. Derlet, J. Vijayakumar, J. Cui, N. S. Bingham, A. Kleibert, and L. J. Heyderman, Computational logic with square rings of nanomagnets, Nanotechnology **29**, 265205 (2018).

[10] J. Park, B. L. Le, J. Sklenar, G. W. Chern, J. D. Watts, and P. Schiffer, Magnetic response of brickwork artificial spin ice, Phys. Rev. B **96**, 024436 (2017).

[11] Y. Li, T. X. Wang, Z. T. Hou, H. Y. Liu, X. F. Dai, and G. D. Liu, Thermodynamics and magnetization reversal in artificial brickwork spin ice, Phys. Lett. A. **380**, 2013 (2016).

[12] I. Gilbert, Y. Lao, I. Carrasquillo, L. O'brien, J. D. Watts, M. Manno, C. Leighton, A. Scholl, C. Nisoli, and P. Schiffer, Emergent reduced dimensionality by vertex frustration in artificial spin ice, Nat. Phys. **12**, 162 (2016).

[13] S. H. Skjærvø, C. H. Marrows, R. L. Stamps, and L. J. Heyderman, Advances in artificial spin ice, Nat. Rev. Phys. **2**, 13 (2020).

[14] A. Farhan, A. Scholl, C. F. Petersen, L. Anghinolfi, C. Wuth, S. Dhuey, R. V. Chopdekar, P. Mellado, M. J. Alava, and S. Van Dijken, Thermodynamics of emergent magnetic charge screening in artificial spin ice, Nat. Commun. **7**, 12635 (2016).

[15] E. Mengotti, L. J. Heyderman, A. Fraile Rodríguez, A. Bisig, L. Le Guyader, F. Nolting, and H. B. Braun, Building blocks of an artificial kagome spin ice: Photoemission electron microscopy of arrays of ferromagnetic islands, Phys. Rev. B **78**, 144402 (2008).

[16] Y. Perrin, B. Canals, and N. Rougemaille, Extensive degeneracy, Coulomb phase and magnetic monopoles in artificial square ice, Nature **540**, 410 (2016).

[17] L. F. Yin, D. H. Wei, N. Lei, L. H. Zhou, C. S. Tian, G. S. Dong, X. F. Jin, L. P. Guo, Q. J. Jia, and R. Q. Wu, Magnetocrystalline Anisotropy in Permalloy Revisited, Phys. Rev. Lett. **97**, 067203 (2006).

[18] H. Y. Hwang, Y. Iwasa, M. Kawasaki, B. Keimer, N. Nagaosa, and Y. Tokura, Emergent phenomena at oxide interfaces, Nat. Mater. **11**, 103 (2012).

[19] P. Zubko, S. Gariglio, M. Gabay, P. Ghosez, and J. M. Triscone, Interface physics in complex oxide heterostructures, Annu. Rev. Condens. Matter Phys. **2**, 141 (2011).

[20] Y. Takamura, R. V. Chopdekar, A. Scholl, A. Doran, J. A. Liddle, B. Harteneck, and Y. Suzuki, Tuning magnetic domain structure in nanoscale $La_{0.7}Sr_{0.3}MnO_3$ islands, Nano Lett. **6**, 1287 (2006).

[21] Y. Takamura, E. Folven, J. B. R. Shu, K. R. Lukes, B. Li, A. Scholl, A. T. Young, S. T. Retterer, T. Tybell, and J. K. Grepstad, Spin-Flop Coupling and Exchange Bias in Embedded Complex Oxide Micromagnets, Phys. Rev. Lett. **111**, 107201 (2013).

[22] M. S. Lee, T. A. Wynn, E. Folven, R. V. Chopdekar, A. Scholl, A. T. Young, S. T. Retterer, J. K. Grepstad, and Y. Takamura, Tailoring spin textures in complex oxide micromagnets, ACS Nano **10**, 8545 (2016).

[23] E. J. Kim, J. L. R. Watts, B. Harteneck, A. Scholl, A. Young, A. Doran, and Y. Suzuki, Magnetic domain structure of $La_{0.7}Sr_{0.3}MnO_3$ nanoislands: Experiment and simulation, J. Appl. Phys. **109**, 07D712 (2011).

[24] E. Folven, J. Linder, O. V. Gomonay, A. Scholl, A. Doran, A. T. Young, S. T. Retterer, V. K. Malik, T. Tybell, Y. Takamura, and J. K. Grepstad, Controlling the switching field in nanomagnets by means of domain-engineered antiferromagnets, Phys. Rev. B **92**, 094421 (2015).

[25] R. V. Chopdekar, B. Li, T. A. Wynn, M. S. Lee, Y. Jia, Z. Q. Liu, M. D. Biegalski, S. T. Retterer, A. T. Young, A. Scholl, and Y. Takamura, Nanostructured complex oxides as a route towards thermal behavior in artificial spin ice systems, Phys. Rev. Mater. **1**, 024401 (2017).

[26] J. Mizusaki, N. Mori, H. Takai, Y. Yonemura, H. Minamiue, H. Tagawa, M. Dokiya, H. Inaba, K. Naraya, T. Sasamoto, and T. Hashimoto, Oxygen nonstoichiometry and defect equilibrium in the perovskite-type oxides $La_{1-x}Sr_xMnO_{3+d}$, Solid State Ionics **129**, 163 (2000).

[27] J. M. Porro, A. Bedoya-Pinto, A. Berger, and P. Vavassori, Exploring thermally induced states in square artificial spin-ice arrays, New J. Phys. **15**, 055012 (2013).

[28] S. Zhang, I. Gilbert, C. Nisoli, G. W. Chern, M. J. Erickson, L. O'Brien, C. Leighton, P. E. Lammert, V. H. Crespi, and P. Schiffer, Crystallites of magnetic charges in artificial spin ice, Nature **500**, 553 (2013).

[29] X. Zhang, Y. Lao, J. Sklenar, N. S. Bingham, J. T. Batley, J. D. Watts, C. Nisoli, C. Leighton, and P. Schiffer, Understanding thermal annealing of artificial spin ice, APL Mater. **7**, 111112 (2019).

[30] E. Folven, T. Tybell, A. Scholl, A. Young, S. T. Retterer, Y. Takamura, and J. K. Grepstad, Antiferromagnetic domain reconfiguration in embedded $LaFeO_3$ thin film nanostructures, Nano Lett. **10**, 4578 (2010).

[31] L. M. Berndt, V. Balbarin, and Y. Suzuki, Magnetic anisotropy and strain states of (001) and (110) colossal magnetoresistance thin films, Appl. Phys. Lett. **77**, 2903 (2000).

[32] A. Doran, M. Church, T. Miller, G. Morrison, A. T. Young, and A. Scholl, Cryogenic PEEM at the advanced light source, J. Electron Spectrosc. Relat. Phenom. **185**, 340 (2012).

[33] G. van der Laan and A. I. Figueroa, X-ray magnetic circular dichroism - a versatile tool to study magnetism, Coord. Chem. Rev. **277**, 95 (2014).

[34] G. Bradski, The OpenCV Library, Dr. Dobb's J. Softw. Tools **25**, 120 (2000).

[35] Y. Rubner, C. Tomasi, and L. J. Guibas, Earth mover's distance as a metric for image retrieval, Int. J. Comput. Vis. **40**, 99 (2000).

[36] E. Östman, H. Stopfel, I. A. Chioar, U. B. Arnalds, A. Stein, V. Kapaklis, and B. Hjörvarsson, Interaction modifiers in artificial spin ices, Nat. Phys. **14**, 375 (2018).

[37] A. Vansteenkiste, J. Leliaert, M. Dvornik, M. Helsen, F. Garcia-Sanchez, and B. Van Waeyenberge, The design and verification of MuMax3, AIP Adv. **4**, 107133 (2014).

[38] See Supplemental Material at http://link.aps.org/supplemental/10.1103/PhysRevApplied.17.064057 for representative XMCD PEEM images and MSFs of brickwork and square ASIs A–H, MSF analysis of brickwork ASIs, XMCD PEEM images of brickwork ASI G before and after *in situ* thermal demagnetization, and diagrams of the first and second nearest neighbors in brickwork and square ASIs.

[39] E. Y. Tsymbal, Theory of magnetostatic coupling in thin-film rectangular magnetic elements, Appl. Phys. Lett. **77**, 2740 (2000).

[40] R. Álvarez-Sánchez, J. L. Costa-Krämer, and F. Briones, Analytical model for shape anisotropy in thin-film nanostructured arrays: Interaction effects, J. Magn. Magn. Mater. **307**, 171 (2006).

[41] A. M. Kane, I.-T. Chiu, N. J. Ahlm, R. V. Chopdekar, A. T. N'Diaye, E. Arenholz, A. Mehta, V. Lauter, and Y. Takamura, Controlling magnetization vector depth profiles of $La_{0.7}Sr_{0.3}CoO_3/La_{0.7}Sr_{0.3}MnO_3$ exchange spring bilayers via interface reconstruction, ACS Appl. Mater. Interfaces **12**, 45437 (2020).

[42] A. M. Kane, R. V. Chopdekar, A. T. N'Diaye, A. Scholl, E. Arenholz, A. Mehta, and Y. Takamura, Decoupling exchange bias and coercivity enhancement in a perovskite oxide exchange spring bilayer, Phys. Rev. Mater. **3**, 014413 (2019).

[43] W. Eerenstein, M. Wiora, J. L. Prieto, J. F. Scott, and N. D. Mathur, Giant sharp and persistent converse magnetoelectric effects in multiferroic epitaxial heterostructures, Nat. Mater. **6**, 348 (2007).

[44] B. Náfrádi, P. Szirmai, M. Spina, A. Pisoni, X. Mettan, N. M. Nemes, L. Forró, and E. Horváth, Tuning ferromagnetism at room temperature by visible light, Proc. Natl. Acad. Sci. U. S. A. **117**, 6417 (2020).